Russian Journal of Earth Sciences Online ISSN: 1681-1208

Special Issue: "Kamchatka Earthquake M 8.8 on July 29, 2025"

Built-Up Strain and the Predictability of the July 29(30), 2025 Kamchatka Earthquake

I. S. Vladimirova*[,1,2], I. A. Vorobieva[1], K. V. Krushelnitskii[1], G. M. Steblov[1], and P. N. Shebalin[1,3]

[1] Institute of Earthquake Prediction Theory and Mathematical Geophysics of Russian Academy of Sciences, Moscow, Russian Federation
[2] Shirshov Institute of Oceanology of Russian Academy of Sciences, Moscow, Russian Federation
[3] Geophysical Center of the Russian Academy of Sciences, Moscow, Russian Federation
* **Correspondence to:** Irina Vladimirova, ir.s.vladimirova@yandex.ru

Abstract: The July 29(30), 2025 Kamchatka earthquake occurred only 73 years after the major November 4, 1952 event in the same subduction zone, highlighting the relatively short interval between two large ruptures in this segment. The 2025 earthquake (M_W 8.8) ruptured approximately 480 km of the Kuril-Kamchatka Trench, generating a moderate tsunami with maximum recorded wave heights of ~4–5 m, smaller than expected for an event of this magnitude. Based on synthetic earthquake catalogs generated using stochastic modeling of background seismicity and ETAS-type aftershock sequences, the most likely location and depth of a future earthquake with $M_W \geq 7.7$ were identified as early as October 2024 in this region. Moreover, our prior calculations of accumulated seismogenic potential in this segment of the subduction zone, based on 28 years of continuous GNSS observations, indicated that an earthquake of this magnitude was indeed possible. GNSS-derived estimates of accumulated elastic strain indicate that the July 29(30), 2025 mainshock released the majority of the stored seismogenic potential, while large September 13 and 18, 2025 aftershocks likely redistributed stress along the subduction interface, partially releasing previously accumulated strain. Estimates of remaining seismogenic potential suggest that areas north of the 2025 rupture remain capable of producing large earthquakes ($M_W \approx 8$), emphasizing the importance of continuous geodetic and seismic monitoring, and demonstrating that combining long-term probabilistic seismic modeling with GNSS-based strain measurements can improve the anticipation of large earthquakes.

Keywords: Kuril–Kamchatka subduction zone, 2025 Kamchatka megathrust earthquake, earthquake forecasting, probabilistic seismic modeling, interplate coupling, seismogenic potential, numerical modeling, GNSS

Citation: Vladimirova I. S., Vorobieva I. A., Krushelnitskii K. V., Steblov G. M., and Shebalin P. N. (2026), Built-Up Strain and the Predictability of the July 29(30), 2025 Kamchatka Earthquake, *Russian Journal of Earth Sciences*, 26, ES2004, EDN: TSREMA, https://doi.org/10.2205/2026es001114

Research Article

Received: February 2, 2026
Accepted: May 25, 2026
Published: July 1, 2026

1. Introduction

The Kamchatka region lies within a highly active subduction zone, where the Pacific lithospheric plate subducts beneath the Okhotsk plate at a rate of ~80 mm/year [*DeMets et al.*, 2010]. Such rapid convergence promotes continuous strain accumulation along the plate interface, leading to frequent large earthquakes and making the region one of the most seismically active and hazardous on Earth (Figure 1a). Despite this high background seismicity, the occurrence of the July 29(30), 2025 earthquake was unexpected, highlighting the complex nature of strain accumulation and release in this subduction segment.

On July 29, 2025, at 23:24:52 UTC (July 30, 2025, 11:24:52 local time, Kamchatka), a devastating earthquake with a magnitude of M_W 8.8 [*United States Geological Survey (USGS)*, 2025] struck off the eastern coast of Kamchatka, making it the strongest event

in the region since the catastrophic November 4, 1952, North Kuril earthquake (M_W 9.0–9.2) [*Dolgikh et al.*, 2025; *Kostenko et al.*, 2025; *Mikhailov et al.*, 2025]. According to estimates by the United States Geological Survey (USGS), the 2025 Kamchatka earthquake rupture extended approximately 480 km southwestward along the Kuril-Kamchatka Trench. Despite the earthquake's high magnitude, the resulting tsunami remained surprisingly moderate, with a maximum recorded height of only ~4–5 m along the coasts of Kamchatka and the Kuril Islands [*Kostenko et al.*, 2025].

In the year preceding the 2025 mainshock, this segment of the subduction zone was characterized by increased seismic activity. On August 18, 2024, an earthquake of M_W 7.0 occurred in this area, followed by a series of events on July 20, 2025, the largest reaching M_W 7.5. The occurrence of these foreshocks suggests that the fault was approaching a critical state, with accumulated tectonic stresses nearing the strength limit of the rocks and local stress redistribution taking place near the future mainshock rupture zone.

The 2025 earthquake occurred only 73 years after the 1952 megathrust earthquake. Although such a powerful earthquake happened unexpectedly, satellite geodetic measurements had shown that sufficient seismogenic potential had accumulated in this portion of the subduction zone to allow for an event of this magnitude (M_W 8.6–8.7). Moreover, statistical analysis of background seismicity, using synthetic earthquake catalogs and aftershock modeling, had already identified the most probable location and depth of a future $M_W \geq 7.7$ earthquake in this region. These findings were summarized in an internal report titled "A set of works for a comprehensive expert opinion on the most probable location of a strong ($M > 7.7$) earthquake in the Kamchatka Territory, including an assessment of the maximum accumulated seismic moment of the most probable scenario of a strong earthquake, over the next 10 years" issued in October 2024, demonstrating that combining geodetic monitoring with probabilistic seismic analysis can provide actionable guidance for anticipating large earthquakes along active subduction zones.

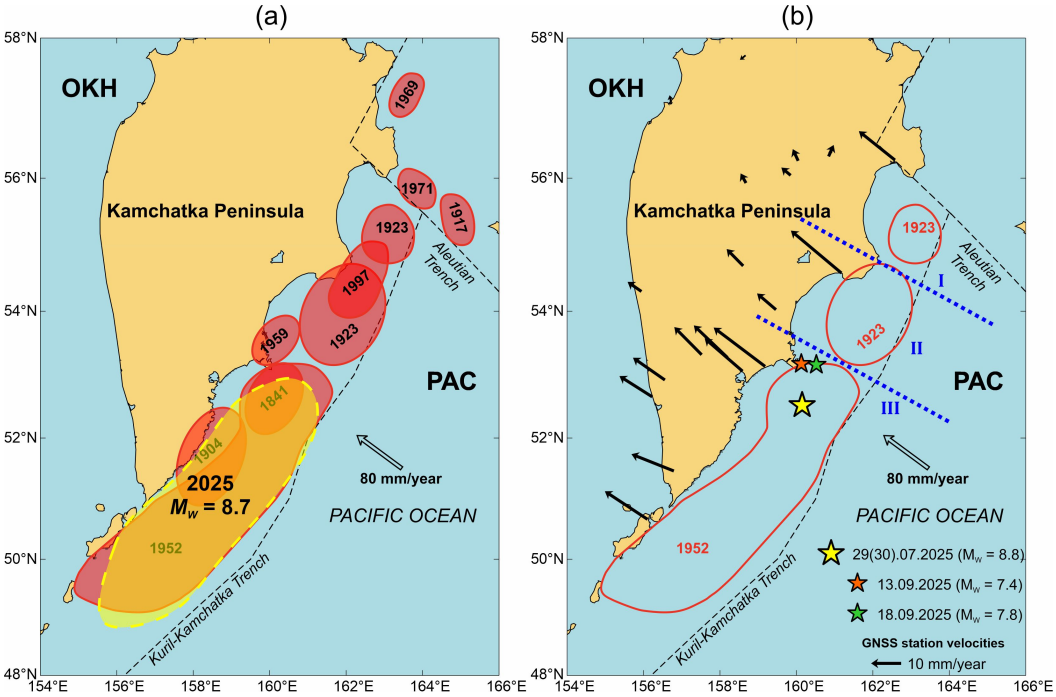

Figure 1. Seismicity of Kamchatka: (a) Red ellipses indicate the source zones of the strongest historical earthquakes ($M \geq 7.7$) after Fedotov and Solomatin [*Fedotov and Solomatin*, 2015], and the yellow dashed ellipse marks the source area of the 2025 Kamchatka earthquake. (b) Epicenters of major historical earthquakes used for segmentation of the subduction zone, segmentation boundaries shown by blue dashed lines, the July 29(30), 2025 mainshock (yellow star), and the two largest aftershocks on September 13 and 18, 2025 (orange and green stars, respectively). PAC – Pacific lithospheric plate; OKH – Okhotsk lithospheric plate.

2. GNSS-Based Estimation of Interplate Coupling and Built-Up Strain

Analysis of modern satellite geodetic measurements enables modeling of the kinematics of lithospheric plate motions and assessing the dynamics of stress accumulation in subduction zones. The interplate coupling coefficient φ is commonly used to quantify interplate deformation, defined as the ratio of the back-slip velocity of the overriding plate's base $\mathbf{V}_{\text{lock}}$ to the plate convergence rate $\mathbf{V}_{\text{conv}}$ (Figure 2):

$$\varphi = \frac{|\mathbf{V}_{\text{lock}}|}{|\mathbf{V}_{\text{conv}}|}, \quad 0 \le \varphi \le 1,$$

where $\mathbf{V}_{\text{lock}}$ and $\mathbf{V}_{\text{conv}}$ are vectors, and $|\mathbf{V}|$ denotes their magnitude. Back-slip $\mathbf{V}_{\text{lock}}$ is directed opposite to $\mathbf{V}_{\text{conv}}$, so the ratio remains positive. $\varphi = 0$ corresponds to free slip, and $\varphi = 1$ corresponds to full coupling. Mapping φ provides insight into the intensity of elastic stress accumulation along the plate interface.

Following [*Savage*, 1983], the surface velocity $\mathbf{V}_{\text{def}}$ at a point $\mathbf{r}$ is modeled as the convolution of the base back-slip $\mathbf{V}_{\text{lock}}$ at a point $\mathbf{r}_s$ with a Green's function $\mathbf{G}(\mathbf{r}, \mathbf{r}_s)$ along the contact zone S:

$$\mathbf{V}_{\text{def}}(\mathbf{r}) = \iint_S \mathbf{G}(\mathbf{r}, \mathbf{r}_s)\mathbf{V}_{\text{lock}}(\mathbf{r}_s)dS.$$

Here, $\mathbf{r}$ is the position vector of a surface point, and $\mathbf{r}_s$ is a position vector on the plate interface. In the general *Savage* [1983] formulation, $\mathbf{V}_{\text{lock}}(\mathbf{r}_s)$ and $\mathbf{V}_{\text{conv}}$ are three-component vectors (including shear along the interface, thrust/overriding motion, and vertical/extension – compression). In this study, only the horizontal components of GNSS velocities were used, so $\mathbf{V}_{\text{lock}}$ and $\mathbf{V}_{\text{conv}}$ are effectively two-dimensional, representing horizontal motion along the interface, while the vertical component is not constrained.

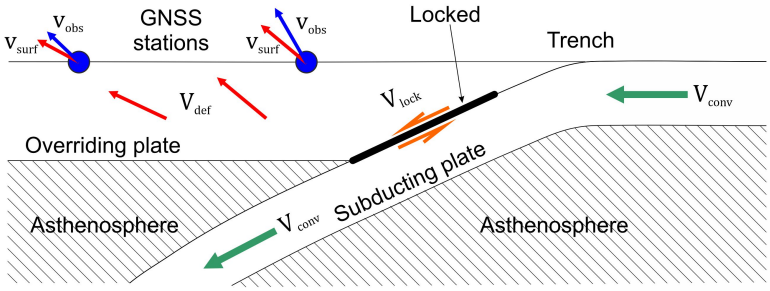

Figure 2. Tectonic motions and resulting deformations in a subduction zone [*Savage*, 1983]. Green arrows – oceanic plate convergence $\mathbf{V}_{\text{conv}}$; orange arrows – normal slip on the locked part of the subduction zone $\mathbf{V}_{\text{lock}}$; red arrows – modeled deformation $\mathbf{V}_{\text{def}}$ and surface component $\mathbf{v}_{\text{surf}}$; blue arrows – observed surface velocities $\mathbf{v}_{\text{obs}}$.

Observed surface velocities $\mathbf{v}_{\text{obs}}$ are compared with modeled velocities $\mathbf{v}_{\text{surf}}$ to solve the inverse problem for $\mathbf{V}_{\text{lock}}$, yielding the distribution of interplate coupling φ. The functional

$$\Phi(\mathbf{V}_{\text{lock}}(\mathbf{r}_s)) = \sum_i \left| \iint_S \mathbf{G}(\mathbf{r}_i, \mathbf{r}_s)\mathbf{V}_{\text{lock}}(\mathbf{r}_s)dS - \mathbf{v}_{obs,i} \right|^2 + \lambda \|\mathbf{V}_{\text{lock}}(\mathbf{r}_s)\|^2$$

is minimized with respect to $\mathbf{V}_{\text{lock}}(\mathbf{r}_s)$, i.e., there exists a solution $\mathbf{V}^*_{\text{lock}}(\mathbf{r}_s)$ such that:

$$\Phi\left(\mathbf{V}^*_{\text{lock}}(\mathbf{r}_s)\right) = \min_{\mathbf{V}_{\text{lock}}(\mathbf{r}_s)} \Phi(\mathbf{V}_{\text{lock}}(\mathbf{r}_s)).$$

Here, λ is a regularization parameter ensuring stability and physical plausibility of the solution. Adequate discretization and λ selection are required for consistency with measurement errors.

Several approaches exist for computing the Green's function. Analytical solutions for a homogeneous elastic half-space are provided by [*Okada*, 1985], while [*Pollitz*, 1996] presents formulations for a layered, spherical elastic Earth. Numerical modeling indicates that neglecting Earth's curvature and stratification can introduce errors of ≥ 20% in surface displacements at large distances from the source [*Steblov et al.*, 2010]. For the Kamchatka Peninsula, where observation points are located more than 150 km from the Kuril-Kamchatka Trench, we adopt a spherically symmetric, radially heterogeneous Earth model (PREM) [*Dziewonski and Anderson*, 1981] to improve computational accuracy. The methodology for modeling geodynamic processes in subduction zones is described in more detail by [*Steblov and Vladimirova*, 2023].

In this study, surface velocities were estimated using 28 years of continuous GNSS observations (1996–2024) from a network of 19 stations (Figure 1b). The velocities of stations within the Kamchatka GNSS network were estimated using a regression-based time series analysis, as described by Nikolaidis [*Nikolaidis*, 2002], designed to account for seasonal, coseismic, and postseismic deformation signals. This method constructs a parametric regression model as a function of time, fitted to the daily coordinate solutions of each station. In the general case, any of the three coordinate components of a station can be represented as:

$$
\begin{aligned}
y(t_i) = a + bt_i + c\sin(2\pi t_i) + d\cos(2\pi t_i) + e\sin(4\pi t_i) + f\cos(4\pi t_i) \\
+ \sum_{j=1}^{n_g} g_j H\left(t_i - \tau_g^j\right) + \sum_{j=1}^{n_h} h_j H\left(t_i - \tau_h^j\right) \\
+ \sum_{j=1}^{n_k} k_j H\left(t_i - \tau_k^j\right) H\left(\tau_k^{j+1} - t_i\right) \cdot t_i \\
+ \sum_{j=1}^{n_l} l_j \ln\left(1 + \frac{t_i - \tau_l^j}{m_j}\right) H\left(t_i - \tau_l^j\right) \\
+ \sum_{j=1}^{n_p} p_j \exp\left(-\frac{t_i - \tau_p^j}{r_j}\right) H\left(t_i - \tau_p^j\right) + \varepsilon_i,
\end{aligned}
$$

where t_i, $i = 1 \ldots N$ are the observation epochs, a is the initial coordinate, b is the linear velocity of station displacement, c, d, e, and f represent annual and semi-annual periodic signals (e.g., seasonal, atmospheric, or oceanic tides), H is the Heaviside function. The terms g_j correspond to offsets due to equipment or software changes at time τ_g^j; h_j are coseismic offsets at time τ_h^j; k_j accounts for changes in linear velocity after earthquakes at τ_k^j. The last two summations represent postseismic transients: logarithmic (afterslip) and exponential (viscoelastic relaxation in the upper mantle and asthenosphere). ε_i denotes measurement noise. An example of applying this regression analysis to GNSS station data from the Kamchatka network is shown in Figure 3.

3. Interplate Coupling and Seismogenic Potential of the Kuril–Kamchatka Megathrust

The resulting distribution of the interplate coupling coefficient φ along the Kuril–Kamchatka subduction zone (Figure 4a) was obtained by solving the inverse problem at discrete points along the plate interface (finite elements) using horizontal GNSS velocities. The discrete solution was regularized to produce a smooth, spatially continuous approximation of the coupling distribution. The strongest coupling and stress accumulation extend along nearly the entire Kamchatka coast, with the plate interface bounded at the top by the trench and at the downdip end by 150 km depth. Exceptionally high coupling ($\varphi \approx 0.8$–1.0) along much of the interplate boundary promotes rapid elastic strain buildup, increasing the risk of large-magnitude earthquakes. This pattern is consistent with the presence of a thin layer of hydrated sediments at the top of subduction zones, which acts as a lubricant and facilitates slip along the shallow interface [*Sorokhtin and Lobkovsky*, 1976].

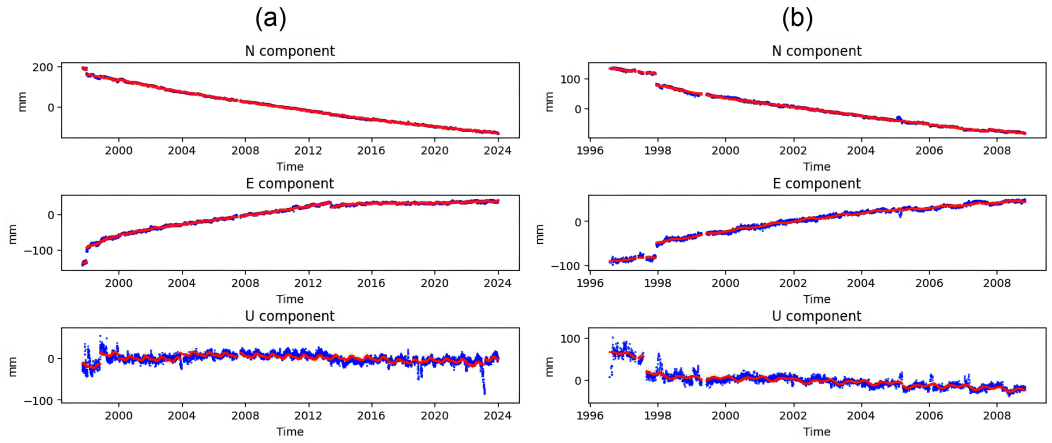

Figure 3. Three-component GNSS time series at (a) _ES1 (Esso village, Kamchatka Krai) and (b) _KLU (Klyuchi settlement, Kamchatka Krai). Blue points represent the observed displacements, while the red lines show the regression model fitted to the data.

Variations in interplate coupling along the Kuril–Kamchatka subduction zone were previously estimated by *Steblov et al.* [2010]. Both their model (Figure 4b) and the present study (Figure 4a) use the same GNSS velocity field but adopt different inverse problem formulations. In the present study, the plate interface geometry was prescribed a priori, and a spatially variable coupling coefficient φ was estimated, allowing partial locking and yielding a continuous distribution of coupling intensity. In *Steblov et al.* [2010], only the downdip extent of full locking was estimated, focusing on the geometry of the locked zone rather than its intensity.

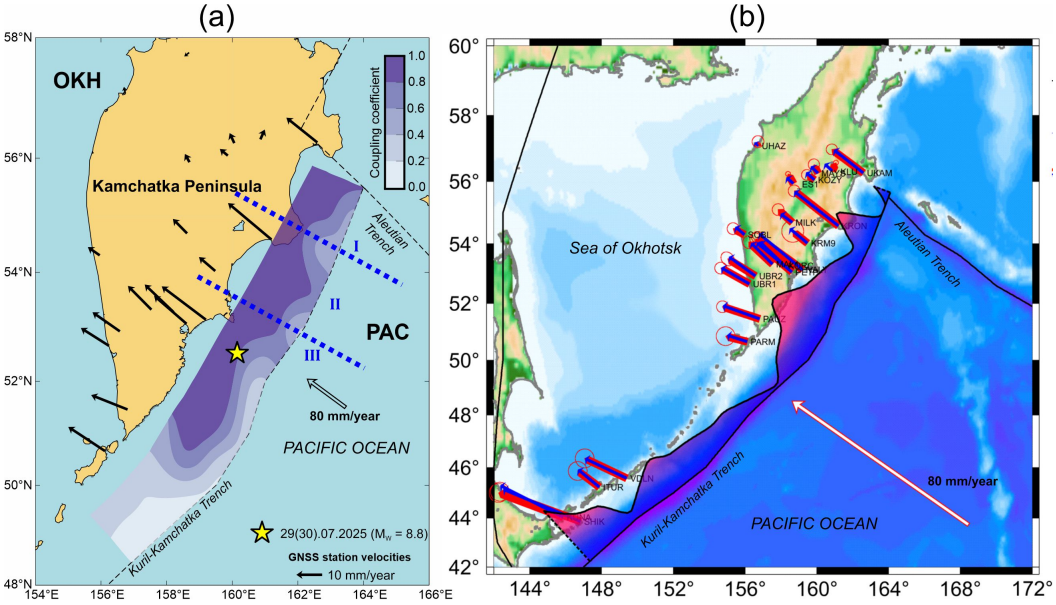

Figure 4. Geometry of interplate coupling along the Kuril–Kamchatka subduction zone: (a) estimated in the present study; (b) obtained in Steblov et al. *Steblov et al.* [2010].

Despite methodological differences, both models consistently delineate a central segment of strong interplate coupling, with reduced locking toward the northern and southern ends of Kamchatka. Notably, the July 29(30), 2025 Kamchatka earthquake occurred precisely within this central segment, with both its epicenter and main rupture zone coinciding with the strongly coupled patch. Local discrepancies, such as near Cape Kronotsky, reflect the intrinsic non-uniqueness of the inverse problem: the coefficient-based

inversion captures gradual variations but is sensitive to smoothing and data resolution, whereas the locking-depth approach imposes quasi-binary constraints, yielding a more stable but less detailed representation. Thus, while first-order coupling patterns are robust and method-independent, second-order variations remain sensitive to the chosen parameterization.

Based on the distribution of interplate coupling obtained in this study, the accumulated seismogenic potential M_0^{accum} was estimated by integrating the product of local slip deficit, shear modulus, and accumulation time over the interplate contact zone:

$$M_0^{\text{accum}} = \mu \iint_S \Delta u(\mathbf{r}_s) T(\mathbf{r}_s) dS,$$

where μ is the shear modulus, $T(\mathbf{r}_s)$ is the local accumulation time since the last major earthquake, and $\Delta u(\mathbf{r}_s)$ is the local slip deficit, $\mathbf{r}_s$ denotes a source point along the subduction interface, and S is the interplate contact zone. The slip deficit $\Delta u(\mathbf{r}_s)$ is related to the back-slip velocity $\mathbf{V}_{\text{lock}}(\mathbf{r}_s)$ and the plate convergence velocity $\mathbf{V}_{\text{conv}}$ through the coupling coefficient $\varphi(\mathbf{r}_s)$:

$$\Delta u(\mathbf{r}_s) = \mathbf{V}_{\text{lock}}(\mathbf{r}_s) T(\mathbf{r}_s) = \varphi(\mathbf{r}_s) \mathbf{V}_{\text{conv}} T(\mathbf{r}_s),$$

The shear modulus was assumed to be $\mu = 40$ GPa, following *Ammon et al.* [2008].

The resulting scalar seismic moment was then converted into moment magnitude following *Hanks and Kanamori* [1979]:

$$M_{\text{W}}^{\text{accum}} = \frac{2}{3}(\log_{10} M_0^{\text{accum}} - 9.1).$$

It is well established that the largest earthquakes tend to recur quasi-periodically in approximately the same segments of a seismogenic zone [e.g., *Bilek and Lay*, 2018]. Taking this into account, and assuming that the spatial pattern of interplate coupling remains sufficiently stable over time, we estimate the amount of elastic energy that has accumulated to date within the rupture areas of past major earthquakes with $M_{\text{W}} \geq 8$. To do this, we conditionally divide the study region into three segments whose boundaries approximately correspond to the rupture zones of the strongest historical earthquakes: two 1923 events and the 1952 North Kuril earthquake (Figure 1b).

Segment I, in the north, is associated with the April 13, 1923 earthquake (M_{W} 7.3–8.2); the accumulated scalar moment since 1923, minus the 1997 Kronotsky earthquake (M_{W} 7.9), is $M_0^{\text{accum}} = 7.20 \times 10^{20}$ N·m ($M_{\text{W}}^{\text{accum}}$ 7.84). Segment II corresponds to the 3 February 1923 earthquake (M_{W} 8.4), with an accumulated moment of $M_0^{\text{accum}} = 1.25 \times 10^{21}$ N·m ($M_{\text{W}}^{\text{accum}}$ 8.1) after subtracting the 1997 release. Segment III, the southernmost, is defined by the 1952 North Kuril earthquake (M_{W} 9.0), which has accumulated $M_0^{\text{accum}} = 0.99 \times 10^{22}$ N·m ($M_{\text{W}}^{\text{accum}}$ 8.63) to date. These findings highlight that the substantial seismogenic potential along this segment of the subduction zone made the occurrence of a large earthquake, such as the 2025 Kamchatka event, an expected outcome. This segmentation-based approach provides a spatially resolved estimate of the seismogenic potential available for future large earthquakes along the Kuril–Kamchatka subduction zone.

On July 29(30), 2025, a megathrust earthquake with M_{W} 8.8 occurred within the southernmost Segment III. This event likely released the majority of the accumulated elastic strain in this segment. Furthermore, in September 2025, two of the largest aftershocks (September 13, 2025, M_{W} 7.4 and September 18, 2025 M_{W} 7.4) occurred in the northern part of Segment III, near the Shipunsky Peninsula, directly along the boundary of the main 29(30) July rupture. These aftershocks probably contributed to the additional release of elastic strain in the northern portion of the mainshock rupture area. However, if we assume that the main displacements caused by the September aftershocks, which occurred essentially along the boundary between Segments II and III, primarily affected Segment II, the accumulated scalar seismic moment in this segment would be reduced

from $M_0^{\text{accum}} = 1.25 \times 10^{21}$ N·m to approximately $M_0^{\text{accum}} \approx 3.91 \times 10^{20}$ N·m, corresponding to a moment magnitude of M_W^{accum} 7.66. This indicates that a substantial portion of the previously stored elastic strain in Segment II was likely released during these aftershocks, emphasizing the significant role of post-mainshock activity in redistributing stress along the subduction zone.

4. Statistical Analysis of the Most Probable Location of the Epicenter of a Next Large Earthquake

Over the past 40 years, earthquake data have accumulated in the Kamchatka region with significantly greater accuracy than in the previous period [*Chebrov et al.*, 2013]. This makes it possible to apply statistical tools to seismic modeling without introducing subjective information (regional boundaries, acceptable parameter value ranges, etc.). A convenient form of model representation is a synthetic earthquake catalog generated for an arbitrary time interval. This form allows for the inclusion in the model of earthquake aftershocks, which are typically ignored in seismic hazard assessment tasks. Aftershocks are important in seismic risk assessment tasks. Every earthquake, even a small one, contributes to a decrease in the seismic resistance of buildings, and aftershocks make a significant contribution to the cumulative effect of earthquake impacts.

The main assumption in modeling is the fulfillment of the Gutenberg–Richter law:

$$N(M \geq m) = 10^{A_{M_c} - b(m - M_c)},$$

where $N(M \geq m)$ is the number of events with magnitude m or greater, M_c is the completeness magnitude, A_{M_c} and b are parameters. We normalize the number to one year and the area of 100 km^2.

As part of the internal report mentioned above, a synthetic earthquake catalog for Kamchatka was constructed in October 2024 using the methodology of [*Shebalin et al.*, 2024]. This same methodology had already been used to create a synthetic earthquake catalog for the eastern sector of the Russian Arctic [*Shebalin et al.*, 2025]. The main advantage of this methodology is its complete transparency. Using the gridded earthquake catalog, local estimates of seismic regime parameters (the Gutenberg–Richter law parameters and the average number of direct aftershocks per event in a relative magnitude range) and regional estimates of the Gutenberg–Richter and Omori law parameters are made. A catalog of mainshocks is then generated.

In the region under consideration, seismicity can be divided into three types (excluding weak volcanic seismicity): interplate, intraslab, and surface. The hypocenters for these three seismicity types differ in depth, so seismic regime parameters were determined separately, as well as parameters for the Commander Islands region. The values of the A_{M_c} and b are mapped in Figure 5.

Under the assumption of independence, random intervals between events in the region are sequentially generated, and the event magnitude is determined using the regional Gutenberg–Richter law. Using local estimates of A_{M_c} and b, a table of normalized event frequency values of the found magnitude is calculated. A random uniformly distributed number is then generated again, which is used to find the regular grid cell for which, in an ordered sequence of cells, the sum of the normalized frequency values is closest to the generated number. Within the cell, more precise coordinates can also be determined using a random number generator. If necessary, and if a depth distribution model is available, a hypocenter depth can also be generated. If the event magnitude is above a specified threshold, the hypocenter position can be determined within a limited space defined by additional conditions, such as the results of recognizing the large earthquakes-prone areas. In this case, this restriction was not imposed, as the hypothesis of the absence of a preferred location for the hypocenters of strong earthquakes was adopted for Kamchatka.

The next step is generating aftershock sequences using the ETAS-e model [*Shebalin et al.*, 2020]. For each mainshock and then each aftershock, the ETAS-e model generates a certain number of aftershocks. Unlike the standard ETAS model, this model, in accordance

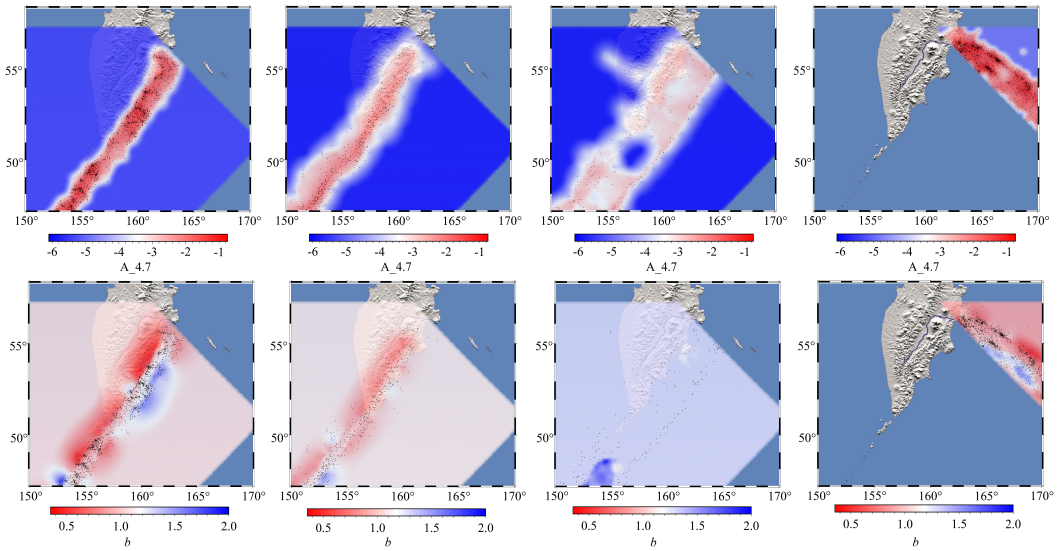

Figure 5. Maps of the parameters A_{M_c} (top row) and b (bottom row): for interplate, intraslab, surface types of seismicity and for Commander Islands from left to right, respectively.

with the productivity law [*Shebalin et al.*, 2020], assumes that the number of aftershocks over a relative magnitude range has an exponential distribution (in the standard model, a Poisson distribution). Because of this, the most probable number of aftershocks is 0, and aftershock sequences always converge.

The objective of the October 2024 study was to find the most likely locations for the epicenter of an earthquake with a magnitude 7.7 or greater. Using the synthetic catalog and direct calculation of the recurrence rate, local estimates of the expected number of a magnitude 7.7 or greater earthquakes were calculated in cells 0.1×0.1 degrees of a regular grid over a 1-year period (Figure 6). The maxima of these estimates are shown in Figure 7. The figure also shows the epicenters of the July 29, 2025, $M = 8.8$ earthquake and its (possible) aftershock on September 18, 2025, $M = 7.8$; they are located close to the estimated maximum.

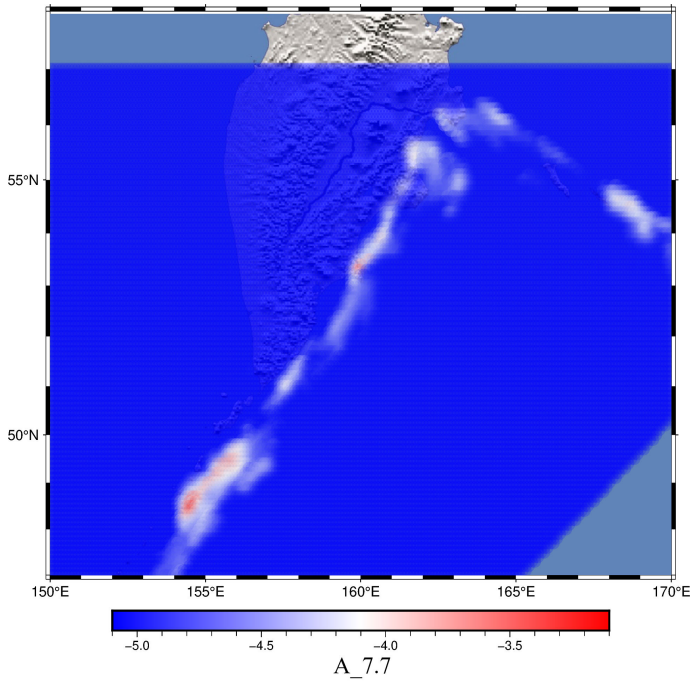

Figure 6. Logarithm of number of earthquakes with magnitude ≥ 7.7 in a cell $0.1° \times 0.1°$ per year.

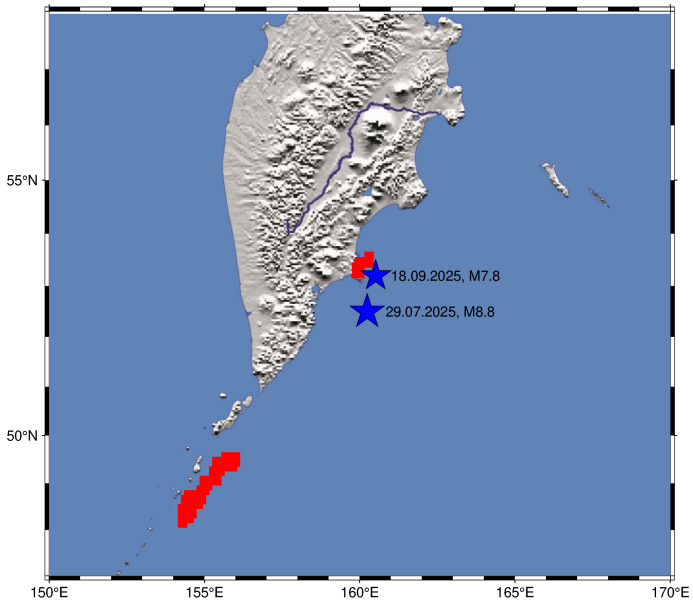

Figure 7. Maxima of estimated expected number of earthquakes with magnitude ≥ 7.7 per time and space units (red squares) and epicenters of the July 29(30), 2025, M = 8.8 and the September 18, 2025, M = 7.8 earthquakes (stars).

5. Seismic Hazard and Post-Earthquake Geodetic Monitoring

Given the high seismic hazard of the Kamchatka Peninsula and the potential for significant stress accumulation along the Kuril–Kamchatka subduction zone, continuous monitoring of crustal deformation is critical to understand the evolving strain field and to improve earthquake hazard assessments.

To improve the precision of deformation and energy-budget estimates for the Kamchatka region after the 2025 megathrust event, new geodetic displacement data are required and must be incorporated within a single, consistently re-adjusted network solution. Large coseismic offsets and prolonged postseismic transients following a M_W 8+ earthquake produce coordinate and velocity changes that are significant even at distances of hundreds of kilometers; consequently, independent epoch-by-epoch solutions are not directly comparable unless all stations are reprocessed together in a common reference frame. A correct treatment therefore requires comprehensive reprocessing and simultaneous adjustment (re-leveling/re-normal equation combination) of all regional GNSS sites used in the study, and construction of a regional realization rigidly tied to the International Terrestrial Reference Frame (ITRF) so that epoch-to-epoch displacements reflect true geophysical signals rather than datum shifts or network drifts. Similar workflows – intensive post-event GNSS reprocessing, network densification, and ITRF-consistent re-adjustment – were implemented after several recent megathrust earthquakes: (a) the 2011 Tohoku earthquake, where GEONET data were kinematically reprocessed and time-variable slip and postseismic deformation were re-estimated [*Iinuma*, 2018; *Nishimura et al.*, 2011]; (b) the 2010 M_W 8.8 Maule earthquake in Chile, involving extensive GNSS campaigns, re-analysis, and development of a unified regional solution [see *Klein et al.*, 2022; *Lin et al.*, 2013]; and (c) the 2004 Sumatra–Andaman earthquake, which required regional GNSS densification and reprocessing to resolve long-term postseismic signals and update regional velocities [e.g., *Kreemer et al.*, 2006]. Implementing the same approach in Kamchatka will ensure that estimates of coseismic offsets, postseismic relaxation, and accumulated elastic strain (and derived energy budgets) are physically meaningful and directly comparable across epochs.

6. Conclusion

The July 29(30), 2025 Kamchatka earthquake – unexpected given the relatively short interval since the 1952 megathrust event – underscores the critical role of interplate

coupling in long-term strain accumulation and its control over the seismic cycle in this subduction zone. Our GNSS-based calculations of accumulated seismogenic potential indicated that an earthquake of this magnitude could have been anticipated in this segment of the Kuril-Kamchatka subduction zone. Seismicity patterns derived from synthetic earthquake catalogs, which simulate both background events and ETAS-modeled aftershock sequences, allowed the identification, already in October 2024, of the most probable location and depth of a future $M_W \geq 7.7$ earthquake.

The July 29(30), 2025 mainshock (M_W 8.8) occurred near this forecasted maximum, releasing the majority of the stored elastic strain. Subsequent large aftershocks on September 13 and 18, 2025 (M_W 7.4 and M_W 7.8, respectively) near the boundary of the July 29(30), 2025 rupture likely redistributed stress along the subduction interface, partially releasing previously accumulated strain. Our estimates suggest that regions immediately north of the 2025 rupture, particularly between the Kronotsky and Shipunsky Peninsulas, still remain capable of generating large earthquakes ($M_W \approx 8$).

The consistency between the probabilistic seismicity forecast and the GNSS-derived strain accumulation estimates highlights the importance of combining long-term statistical earthquake modeling with continuous geodetic monitoring for anticipating major megathrust events. Moreover, the occurrence of the mainshock and the subsequent large aftershocks necessitates a comprehensive reprocessing and re-estimation of GNSS velocities, offsets, and postseismic signals. Updated GNSS solutions will be essential for reconstructing the new deformation field, reassessing interplate coupling, and determining the revised distribution of seismogenic potential along the Kuril–Kamchatka margin.

Together, these results show that only the integration of modern satellite geodesy, physics-based strain accumulation modeling, and probabilistic seismicity forecasts can provide a robust basis for assessing evolving seismic and tsunami hazards in this highly active subduction zone.

Acknowledgments. The work was carried out within the framework of the State Assignment of the IETP RAS (theme No. FMWW-2024-0006 and theme No. FMWW-2024-0010 in the field of "Volcanology and Seismology of Kamchatka," as part of the integrated interagency program for the study and development of the unique territory of the Kamchatka krai "Third Kamchatka Expedition"), as well as within the framework of the State Assignment of the IO RAS (theme No. FMWE-2024-0018) and the State Assignment of the GC RAS. We express our sincere gratitude to Inessa A. Vorobieva (PhD in Physics and Mathematics, Leading Researcher, Institute of Earthquake Prediction Theory and Mathematical Geophysics, Russian Academy of Sciences) for her valuable contribution to this study.

In memoriam: Inessa A. Vorobieva (1960–2026). Her research spanned geophysics, seismology, and geodynamics. She passed away on February 23, 2026.

References

Ammon C. J., Kanamori H. and Lay T. A great earthquake doublet and seismic stress transfer cycle in the central Kuril islands // Nature. — 2008. — Vol. 451, no. 7178. — P. 561–565. — https://doi.org/10.1038/nature06521

Bilek S. L. and Lay T. Subduction zone megathrust earthquakes // Geosphere. — 2018. — Vol. 14, no. 4. — P. 1468–1500. — https://doi.org/10.1130/ges01608.1

Chebrov V. N., Droznin D. V., Kugaenko Yu. A., et al. The system of detailed seismological observations in Kamchatka in 2011 // Journal of Volcanology and Seismology. — 2013. — Vol. 7, no. 1. — P. 16–36. — https://doi.org/10.1134/s0742046313010028

DeMets C., Gordon R. G. and Argus D. F. Geologically current plate motions // Geophysical Journal International. — 2010. — Vol. 181, no. 1. — P. 1–80. — https://doi.org/10.1111/j.1365-246x.2009.04491.x

Dolgikh G. I., Kulchin Yu. N., Dolgikh S. G., et al. Deformation Anomalies of the Tsunamigenic Earthquake of July 29, 2025 // Doklady Earth Sciences. — 2025. — Vol. 525, no. 2. — P. 1–3. — https://doi.org/10.1134/s1028334x2560879x

Dziewonski A. M. and Anderson D. L. Preliminary reference Earth model // Physics of the Earth and Planetary Interiors. — 1981. — Vol. 25, no. 4. — P. 297–356. — https://doi.org/10.1016/0031-9201(81)90046-7

Fedotov S. A. and Solomatin A. V. The long-term earthquake forecast for the Kuril-Kamchatka island arc for the September 2013 to August 2018 period; the seismicity of the arc during preceding deep-focus earthquakes in the sea of Okhotsk (in 2008, 2012, and 2013 at M = 7.7, 7.7, and 8.3) // Journal of Volcanology and Seismology. — 2015. — Vol. 9, no. 2. — P. 65–80. — https://doi.org/10.1134/s0742046315020025

Hanks T. C. and Kanamori H. A moment magnitude scale // Journal of Geophysical Research: Solid Earth. — 1979. — Vol. 84, B5. — P. 2348–2350. — https://doi.org/10.1029/jb084ib05p02348

Iinuma T. Postseismic Uplift Along the Pacific Coast of Tohoku and Kanto Districts Associated with the 2011 off the Pacific Coast of Tohoku Earthquake // Journal of Disaster Research. — 2018. — Vol. 13, no. 3. — P. 496–502. — https://doi.org/10.20965/jdr.2018.p0496

Klein E., Vigny C., Nocquet J.-M., et al. A 20 year-long GNSS solution across South-America with focus in Chile // BSGF - Earth Sciences Bulletin. — 2022. — Vol. 193. — P. 5. — https://doi.org/10.1051/bsgf/2022005

Kostenko I. S., Zaytsev A. I. and Pelinovsky E. N. Tsunami on July 29 (30), 2025 in the Kamchatka-Kuril Zone: Instrumental Observation and Modeling // Doklady Earth Sciences. — 2025. — Vol. 525, no. 2. — https://doi.org/10.1134/s1028334x25608648

Kreemer C., Blewitt G., Hammond W. C., et al. Global deformation from the great 2004 Sumatra-Andaman Earthquake observed by GPS: Implications for rupture process and global reference frame // Earth, Planets and Space. — 2006. — Vol. 58, no. 2. — P. 141–148. — https://doi.org/10.1186/bf03353370

Lin Yu.-N., Sladen A., Ortega-Culaciati F., et al. Coseismic and postseismic slip associated with the 2010 Maule Earthquake, Chile: Characterizing the Arauco Peninsula barrier effect // Journal of Geophysical Research: Solid Earth. — 2013. — Vol. 118, no. 6. — P. 3142–3159. — https://doi.org/10.1002/jgrb.50207

Mikhailov V. O., Konvisar A. M., Smirnov V. B., et al. The Rupture Surface Model of the July 29, 2025 Mw 8.8 Kamchatka Earthquake Based on Satellite Geodesy and Interferometry Data // Doklady Earth Sciences. — 2025. — Vol. 525, no. 2. — https://doi.org/10.1134/s1028334x25608752

Nikolaidis R. Observation of Geodetic and Seismic Deformation with the Global Positioning System : PhD thesis / Nikolaidis R. — San Diego, 2002. — 305 p.

Nishimura T., Munekane H. and Yarai H. The 2011 off the Pacific coast of Tohoku Earthquake and its aftershocks observed by GEONET // Earth, Planets and Space. — 2011. — Vol. 63, no. 7. — P. 631–636. — https://doi.org/10.5047/eps.2011.06.025

Okada Y. Surface deformation due to shear and tensile faults in a half-space // Bulletin of the Seismological Society of America. — 1985. — Vol. 75, no. 4. — P. 1135–1154. — https://doi.org/10.1785/bssa0750041135

Pollitz F. F. Coseismic Deformation From Earthquake Faulting On A Layered Spherical Earth // Geophysical Journal International. — 1996. — Vol. 125, no. 1. — P. 1–14. — https://doi.org/10.1111/j.1365-246x.1996.tb06530.x

Savage J. C. A dislocation model of strain accumulation and release at a subduction zone // Journal of Geophysical Research: Solid Earth. — 1983. — Vol. 88, B6. — P. 4984–4996. — https://doi.org/10.1029/jb088ib06p04984

Shebalin P. N., Baranov S. V., Vorobieva I. A., et al. Seismicity Modeling in Tasks of Seismic Hazard Assessment // Doklady Earth Sciences. — 2024. — Vol. 515, no. 1. — P. 514–525. — https://doi.org/10.1134/s1028334x23603115

Shebalin P. N., Gvishiani A. D., Malyutin P. A., et al. A Synthetic Earthquake Catalog for the Eastern Sector of the Russian Arctic Zone // Journal of Volcanology and Seismology. — 2025. — Vol. 19, no. 2. — P. 113–126. — https://doi.org/10.1134/s0742046325700083

Shebalin P. N., Narteau C. and Baranov S. V. Earthquake productivity law // Geophysical Journal International. — 2020. — Vol. 222, no. 2. — P. 1264–1269. — https://doi.org/10.1093/gji/ggaa252

Sorokhtin O. G. and Lobkovsky L. I. Mechanism for pulling of sediments in subduction zone of lithospheric plates // Izvestiya of the Academy of Sciences of the USSR. Physics of the Solid Earth. — 1976. — Vol. 12, no. 5. — P. 3–10.

Steblov G. and Vladimirova I. Geodetic Inversions and Applications in Geodynamics // Applications of Data Assimilation and Inverse Problems in the Earth Sciences. — Cambridge : Cambridge University Press, 2023. — P. 278–292. — https://doi.org/10.1017/9781009180412.019

Steblov G. M., Vasilenko N. F., Prytkov A. S., et al. Dynamics of the Kuril-Kamchatka subduction zone from GPS data // Izvestiya, Physics of the Solid Earth. — 2010. — Vol. 46, no. 5. — P. 440–445. — https://doi.org/10.1134/s1069351310050095

United States Geological Survey (USGS). M 8.8 - 2025 Kamchatka Peninsula, Russia Earthquake. — URL: https://earthquake.usgs.gov/earthquakes/eventpage/us6000qw60 (visited on 11/02/2025).